Research Article

Nano Research
2022, 15(8): 7234–7246

ISSN 1998-0124 CN 11-5974/O4
https://doi.org/10.1007/s12274-022-4552-7

Selenium vacancies enable efficient immobilization and bidirectional conversion acceleration of lithium polysulfides for advanced Li-S batteries

Yuanchang Li[§], Zhenfang Zhou[§], Yong Li, Zhonghua Zhang (✉), Xiaosong Guo, Jing Liu, Changming Mao, Zhenjiang Li, and Guicun Li (✉)

College of Materials Science and Engineering, Qingdao University of Science and Technology, Qingdao 266042, China
[§] *Yuanchang Li and Zhenfang Zhou contributed equally to this work.*

Received: 5 April 2022 / **Revised:** 6 May 2022 / **Accepted:** 16 May 2022

ABSTRACT

Heterostructures composed of oxides and sulfides (nitrides or carbides) show great potential as sulfur host additives because of the strong adoptability of oxides and catalytic capability of sulfides towards the notorious lithium polysulfides (LiPSs). However, the migration and conversion pathway of LiPSs is seriously confined at a localized interface with inadequate active sites. In this work, the introduction of selenium vacancies into VSe_{2-x} has been demonstrated to successfully synergize the adsorbability and catalytic reactions of LiPSs at an integrated functional surface. The N-doped carbon nanosheets-assembled flower architectures embedded with selenium vacancy-rich VSe_{2-x} and partial vanadium oxides have been controllably synthesized and employed as the cathode additives for lithium-sulfur (Li-S) batteries. Both the experiments and first-principle calculations reveal their strong adsorption to LiPSs and their bidirectional catalytic functionality towards the conversion between S_8 and Li_2S. As expected, the charge and discharge kinetics of VSe_{2-x} containing sulfur cathodes is fundamentally improved (an outstanding rate capabilitiy with 693.7 mAh·g^{-1} at 2 C, a remarkable long-term cyclability within 1,000 cycles at 2 C with S loading 2.27 mg·cm^{-2}, and an excellent areal capacity with 3.44 mAh·cm^{-2} within 100 cycles at 0.5 C). This work presents an effective resolution to couple the adsorbability and catalytic reactions of LiPSs at the material design perspective, and the insights on bidirectional catalytic functionality are of vital to develop functional materials for advanced Li-S batteries.

KEYWORDS

lithium-sulfur batteries, selenium vacancies, vanadium selenide, bidirectional catalysis, conversion kinetics

1 Introduction

Due to the advantages of sulfur's superior lithium-ion storage capacity, abundant earth reserves, and no pollution to the environment, rechargeable lithium-sulfur (Li-S) batteries show great potential in revolutionizing the energy storage devices for electric vehicles and grid storage systems in the future [1, 2]. Nevertheless, there are still some problems to be solved before the sulfur cathodes are widely used. As the intermediate products of charge and discharge, lithium polysulfides (LiPSs) are easily soluble in electrolyte and cause shuttle effect, which not only lower the efficient availability of active substances but also result in the serious corrosion of lithium anode [3]. Moreover, the electrical insulation of sulfur (S_8) and lithium sulfide (Li_2S) determines that if they are accumulated too much, the electron and ion transport of the cathode will be seriously affected, which also causes the loss of active substances and reduces utilization efficiency of sulfur [4]. The loss of active substances will lead to the capacity decay of Li-S batteries, while the blockage of electrons and ion channels in cathode and the irreversible corrosion of the anode will lead to the destruction of the electrodes, and greatly shorten the cycle life of the battery. Therefore, it is urgently requested to improve the slow redox kinetics of sulfur cathodes [5–7].

A large number of studies have been carried out to address the slow conversion kinetics and the shuttle effect of LiPSs [8]. To solve the shuttle effect, a barrier layer is effective and can be designed by modifying Li-S cell separator. For example, the rGO@SL/PP separator with sulfonic groups in the porous lignin network has been carefully designed, and the modified membrane effectively blocks the migration of polysulfide anions without affecting lithium-ion penetration [9]. The Janus double-sided ion-conductive and electron-insulating microporous ion-sieving membranes have been synthesized via ZIF-67 [10], effectively inhibiting the shuttle of LiPSs. The separators modified by the cetrimonium bromide/carbon nanotube/$Ti_3C_2T_x$ hybrids also exhibit obvious effects on immobilizing LiPSs [11]. In addition, the construction of protective layer for lithium metal anode, such as two-dimensional (2D) MoS_2 [12], and the design of sulfur cathode additives, such as MgB_2 [13] and other strategies have been widely implemented. Previous works mainly focus on the catalytic conversion of LiPSs to Li_2S_2 [14, 15]. However, during the reaction processes, it is the slowest step that determines the whole reaction step, namely the solid-solid transformation of Li_2S_2 to Li_2S [16]. Rate-control step refers to a mechanism in which if one of the primitive steps proceeds much slower than the others, it

Address correspondence to Zhonghua Zhang, zhangzh@qust.edu.cn; Guicun Li, guicunli@qust.edu.cn

determines the overall reaction rate [17, 18]. At the same time, most of the works primarily focus on the reduction process of sulfur cathodes, whereas it has not been paid sufficient attention to another key oxidation process of Li_2S to S_8 [19].

More recently, some works have investigated both the oxidation and reduction steps of sulfur cathodes in a way of combining adsorbent materials with catalytic materials, such as MoN-VN [20], WS_2-WO_3 [21], VO_2-VN [22], V_2O_3-V_8C_7 [23], etc. These heterojunctions usually consist of two components, the adsorption mainstay and the catalysis mainstay as shown in Scheme 1. Ideally, the adsorption mainstay is responsible for the adsorption of LiPSs, while the catalysis mainstay is responsible for the further conversion of LiPSs, both of which inhibit the shuttle effect and improve the kinetics of Li-S batteries. However, due to the heterotopic nature of the adsorption and catalysis mainstays, there is little space for the simultaneous adsorption and catalytic reactions leading to very limited and localized interfacial reactions [24]. Therefore, it is crucial to construct functional materials that can synergize the adsorbability and catalytic reactions at the electrode scale.

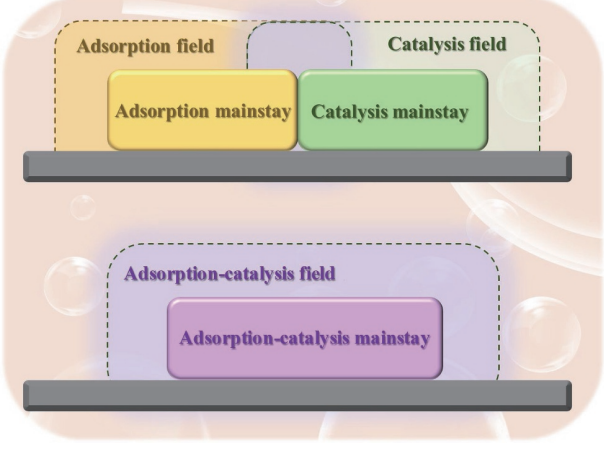

Scheme 1 Schematic diagram of the mechanism of the adsorption mainstay and the catalysis mainstay.

Selenides have been widely used in Li-S batteries due to their catalytic capability for LiPSs and sulfiphilic properties. Typically, ultrafine VSe_2 nanocrystals immobilized on nitrogen-doped graphene have been delicately designed to modify the battery separator to alleviate the shuttling problem of LiPSs, which also show excellent catalytic performances. However, the adsorption capability of VSe_2 (towards Li_2S_6, 1.50 eV) [25] is much weaker than that of V_2O_3 (towards Li_2S_6, 2.18 eV), which may affect the cycle performances of Li-S batteries. Defect engineering [26–28], such as oxygen defect [15] and sulfur defect [29], shows great potential in improving the adsorption and catalytic capabilities towards LiPSs. Therefore, the weak adsorption capability of VSe_2 might be improved by defect engineering, which is seldomly explored to our best knowledge. More importantly, constructing defects in VSe_2 may synergize the adsorbability and catalytic reactions at an integrated functional surface (Scheme 1), simultaneously realizing the effect immobilization and boosted conversion of LiPSs.

In this work, the VSe_{2-x} containing selenium vacancies have been firstly demonstrated to exhibit both strong adsorption and boosted bidirectional catalysis effects towards LiPSs at the molecular level. The nanosheets-assembled flower architectures composed of N-doped carbon materials with a varied proportion of vanadium selenides and vanadium oxides (NC@VO-VSe) have been controllably synthesized and employed as the cathode additives for advanced Li-S batteries. Due to the introduction of selenium vacancies into the VSe_{2-x}, the NC@VO-VSe composites show stronger adsorption towards LiPSs, which effectively inhibit their shuttle effect (Scheme 2). Moreover, NC@VO-VSe composites also exhibit the bidirectional catalysis on both the sulfur reduction reactions and the sulfur oxidation reactions. The energy barriers during the redox conversion process of active substances are greatly reduced as revealed by the density functional theory (DFT) calculations, and the kinetics of charge and discharge of Li-S batteries are fundamentally improved. The cell with S/NC@VO-VSe cathode exhibits improved charge and discharge capacities with an outstanding rate capability of 693.7 $mAh \cdot g^{-1}$ at 2 C, and a remarkable long-term cyclability within 400 cycles at 1 C for S loading of 2.8 $mg \cdot cm^{-2}$. This work couples the

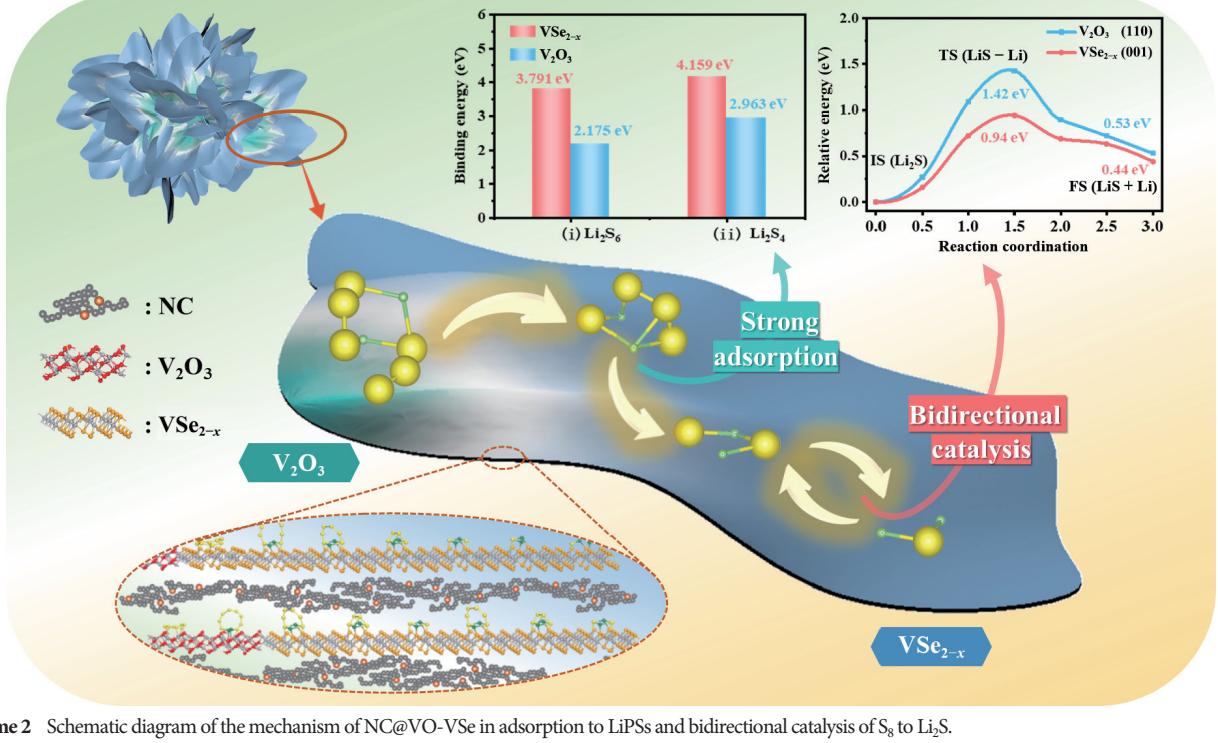

Scheme 2 Schematic diagram of the mechanism of NC@VO-VSe in adsorption to LiPSs and bidirectional catalysis of S_8 to Li_2S.

electrochemical signal with Gibbs free energy change, and the insights pertaining to the bifunctional catalysis are of significance to understand the redox kinetics of Li-S batteries.

2 Experimental

2.1 Materials preparation

2.1.1 Preparation of PVO nanoflower precursor

The polyaniline-V_2O_5 nanoflower precursor (abbreviated as "PVO") precursor was prepared through the intercalation and polymerization reaction of aniline (AN) in V_2O_5. Concretely, 0.12 mL AN was dispersed in 80 mL aqueous solution and stirred on a magnetic stirrer for 5 min. Then, 0.36 g V_2O_5 was dispersed into the above solution with stirring. The pH of the suspension is adjusted to 3 by dropping an appropriate amount of dilute HCl. After ultrasonic treatment for 10 min, the suspension was transferred to a Teflon-lined stainless-steel autoclave and treated at 120 °C for 28 h. Then, the dark gray precipitates can be obtained via rinsing the suspension with deionized water and ethanol for several times, which was treated by centrifugation and then drying at 60 °C in an oven for 12 h.

2.1.2 Preparation of NC@VO-VSe and NC@VO

Typically, the NC@VO-VSe nanoflower was prepared using a simple *in situ* selenization method. In detail, the PVO powder (0.2 g) was moved to a porcelain boat and another porcelain boat with 0.8 g selenium powder was placed on the upstream side of the tube furnace. The furnace with the porcelains was heated up to 350 °C and held for 2 h and then to 500 °C for 2 h with the flow of mixed gases of 5% H_2 and 95% Ar. The obtained black powder was labelled as "NC@VO-VSe". Simultaneously, NC@VO-VSe with different proportions of selenide oxides (labeled as "NC@MVO-VSe" which is the vanadium oxide-rich sample and "NC@VO-MVSe" which is the vanadium selenide-rich sample, respectively) can be obtained by controlling the heating process (NC@MVO-VSe: 500 °C for 4 h; NC@VO-MVSe: 350 °C for 3 h and 500 °C for 1 h). Similarly, NC@VO can be obtained by heating the PVO precursor without selenium powder at 500 °C and held for 4 h with the flow of mixed gases of 5% H_2 and 95% Ar.

2.2 Characterizations

The morphology and microstructure of the materials were characterized via a field emission scanning electron microscopy (SEM, JSM-6700F), energy dispersive spectroscopy (EDS, JEOL-6300F), and a high-resolution transmission electron microscopy (HRTEM, JEM-2100F). The crystal structures of the materials were investigated using a powder X-ray diffraction (XRD, D/MAX/2500PC) with Cu Kα radiation (λ = 1.5406 nm). The X-ray photoelectron spectroscopy (XPS) profiles of the materials were investigated by a Thermo Scientific ESCALAB 250Xi electron spectrometer. Thermogravimetric (TG) curve was conducted on TGA 5500.

2.3 Theoretical modelling

At the beginning of this work, the first-principles calculations [30, 31] have been employed to perform all spin-polarization DFT calculations within the generalized-gradient approximation (GGA) using the Perdew–Burke–Ernzerhof (PBE) [32] formulation. In order to describe the ionic cores, the projected augmented wave (PAW) potentials [33, 34] have been chosen, and valence electrons also have been taken into account using a plane wave basis set with a kinetic energy cutoff of 450 eV. Partial occupancies of the Kohn–Sham orbitals have been determined using the Gaussian smearing method and a width of 0.05 eV. When the energy change was smaller than 10^{-6} eV, the electronic energy can be considered self-consistent, while a geometry optimization can be considered convergent when the energy change was smaller than 0.03 eV·Å^{-1}. In the meantime, the U scheme that has been set as 3.95 eV, need to be applied for the V atoms. We used 15 Å as the vacuum spacing in a direction perpendicular to the plane of the structure for the surfaces, and used 2 × 2 × 1 Monkhorst–Pack k-point sampling for a structure to perform the Brillouin zone integration. In the end, the adsorption energies (E_{ads}) were calculated as $E_{ads} = E_{ad/sub} - E_{ad} - E_{sub}$, where $E_{ad/sub}$, E_{ad}, and E_{sub} are the total energies of the optimized adsorbate/substrate system, the adsorbate in the structure, and the clean substrate, respectively. The free energy was calculated using the equation:

$$G = E + \mathrm{ZPE} - \mathrm{TS}$$

where G, E, ZPE, and TS are the free energy, total energy from DFT calculations, zero point energy, and entropic contributions, respectively. In our calculation, the V_2O_3 (110) and VSe_{2-x} (001) had been established from the bulk structure.

2.4 Electrochemical property measurements

2.4.1 Preparation of the sulfur cathodes

To prepare the sulfur containing vanadium oxide-vanadium selenide coated with nitrogen-doped carbon (S/NC@VO-VSe) sample, the NC@VO-VSe, sulfur powder, and carbon black, in a mass ratio of 1:5:2, were thoroughly ground together, sealed in a Teflon-lined autoclave, and treated at 155 °C for 10 h. The S/C, the S/NC@VO, the S/NC@MVO-VSe, and the S/NC@VO-MVSe were fabricated via the same method. The cathode slurries were prepared via mixing 80 wt.% S/NC@VO-VSe (S/C, S/NC@VO, S/NC@MVO-VSe, or S/NC@VO-MVSe), 10 wt.% carbon black, and 10 wt.% polyvinylidene fluoride (PVDF) in N-methyl-2-pyrrolidone (NMP). In order to get the sulfur cathodes with sulfur loading of 1.45–3.84 mg·cm^{-2}, these slurries were coated on the aluminum (Al) foil and dried under vacuum at 60 °C for 12 h.

2.4.2 The adsorption test of LiPSs

The Li_2S and S with a molar ratio of 5:1 were added to the combined solvents including 1,2-dimethoxyethane (DME) and 1,3-dioxolane (DOL) at a volume ratio of 1:1 to get the Li_2S_6 solution. Then, 30 mg C, NC@VO, and NC@VO-MVSe were respectively immersed in 4 mL of 0.5 mM Li_2S_6 solution and the colors of the initial solutions were recorded. After standing for 4 h, the color of the solution was recorded again to evaluate the adsorption capability of different materials towards Li_2S_6.

2.4.3 The test of reaction kinetics

Sulfur-free materials were employed as the cathodes for the test of reaction kinetics, which were obtained by mixing 40 wt.% sample (NC@VO-VSe, NC@VO, or C) and 40 wt.% C with 10 wt.% PVDF in NMP together to form a slurry. Then the slurry was casted on Al foil and dried under vacuum at 60 °C for 12 h to obtain sulfur-free electrodes that have a mass loading of ~ 6 mg·cm^{-2}. Lithium foil and polypropylene (PP) membrane were served as the anode and separator, respectively. A tetraglyme solution (20 μL) containing 0.5 M Li_2S_6 and 1.0 M lithium bis(trifluoromethanesulfonyl)imide (LiTFSI) was used as the catholyte, while a blank electrolyte (20 μL) was served as the

anolyte. The catholyte and anolyte were dropped onto sulfur-free cathodes and Li anodes, resepctively. The cells should be galvanostatically discharged to 2.05 V. The nucleation and growth of Li_2S can be examined through the potentiostatic discharge of the cells for 50,000 s at 2.05 V.

2.4.4 Assemble and test of symmetrical cells

Sulfur-free cathodes were used as both working electrode and counter electrode of the symmetrical cells. LiTFSI (1.0 M) electrolyte was added to Li_2S_6 solution in DOL/DME (0.1 M, 1:1 v/v) to obtain the electrolyte. The cyclic voltammetry (CV) tests of symmetrical cells were performed at a sweep rate of 10 $mV \cdot s^{-1}$ in the voltage range from −1.5 to 1.5 V.

2.4.5 Electrochemical performances of asymmetric cells

The electrochemical performances of the sulfur cathodes (the as-prepared S/C, S/NC@VO, and S/NC@VO-VSe cathodes) were evaluated using CR-2032 coin-type cells with lithium foil as the anodes, PP membrane as a separator, and DOL/DME (1:1 v/v) solution containing 1.0 M LiTFSI and 1 wt.% lithium nitrate as the electrolyte. The charge/discharge measurements, the CV tests, and electrochemical impedance spectroscopy (EIS) tests were implemented on A LAND CT-2001A system and an Autolab electrochemical workstation, respectively.

3 Results and discussions

3.1 Theoretical modelling

S_8 is converted into Li_2S through a series of reduction processes during the discharge process of Li-S battery, while in the charge process, Li_2S needs to overcome a high energy barrier to decompose into LiS and Li^+, and then transforms into S_8 through subsequent oxidation reaction. The redox kinetics of active substances has a strict one-to-one correspondence with the charge–discharge curve (Fig. 1(a)). In the charging curve of the battery, the initial charging voltage and the overpotential of the charging voltage can reflect the transformation of Li_2S to Li_2S_2 (LiS + Li). The inherent electrical insulation of Li_2S leads to a high energy barrier for conversion from Li_2S to Li_2S_2 (LiS + Li), which is reflected in the initial charging voltage and the overpotential of the charge curve. Among them, the following four challenges should be underlined, electrical insulation of S_8 and Li_2S, shuttling effect of Li_2S_6 and Li_2S_4, slow solid-solid transition from Li_2S_2 to Li_2S, and high decomposition barrier for Li_2S to Li_2S_2 (LiS + Li).

The Gibbs energy profiles for the reduction of LiPSs and decomposition of the Li_2S cluster on VSe_{2-x} (001) and V_2O_3 (110) are shown in Fig. 1(b). Compared with the conversion reaction from S_8 to Li_2S_8 on V_2O_3 (110), the same conversion reaction on VSe_{2-x} (001) releases more energy, indicating the spontaneous exothermic reaction occurs more readily on VSe_{2-x}. This also proves that VSe_{2-x} shows greater kinetic enhancement than V_2O_3 in terms of the conversion reaction from S_8 to Li_2S_8. The facilitated conversion might slightly increase the initial discharge voltage of the battery.

In addition, as indicated by the following four endothermic reactions, the VSe_{2-x} also plays an immeasurable role in further transformation of Li_2S_8. On the one hand, VSe_{2-x} shows the slightly stronger adsorption towards Li_2S_6 (3.791 eV) and Li_2S_4 (4.159 eV) (Fig. 1(c)) than V_2O_3 (towards Li_2S_6: 2.175 eV; towards Li_2S_4: 2.963 eV) and VSe_2 (001) without selenium vacancies (towards Li_2S_6: 1.50 eV) [25]. This result suggests that VSe_{2-x}

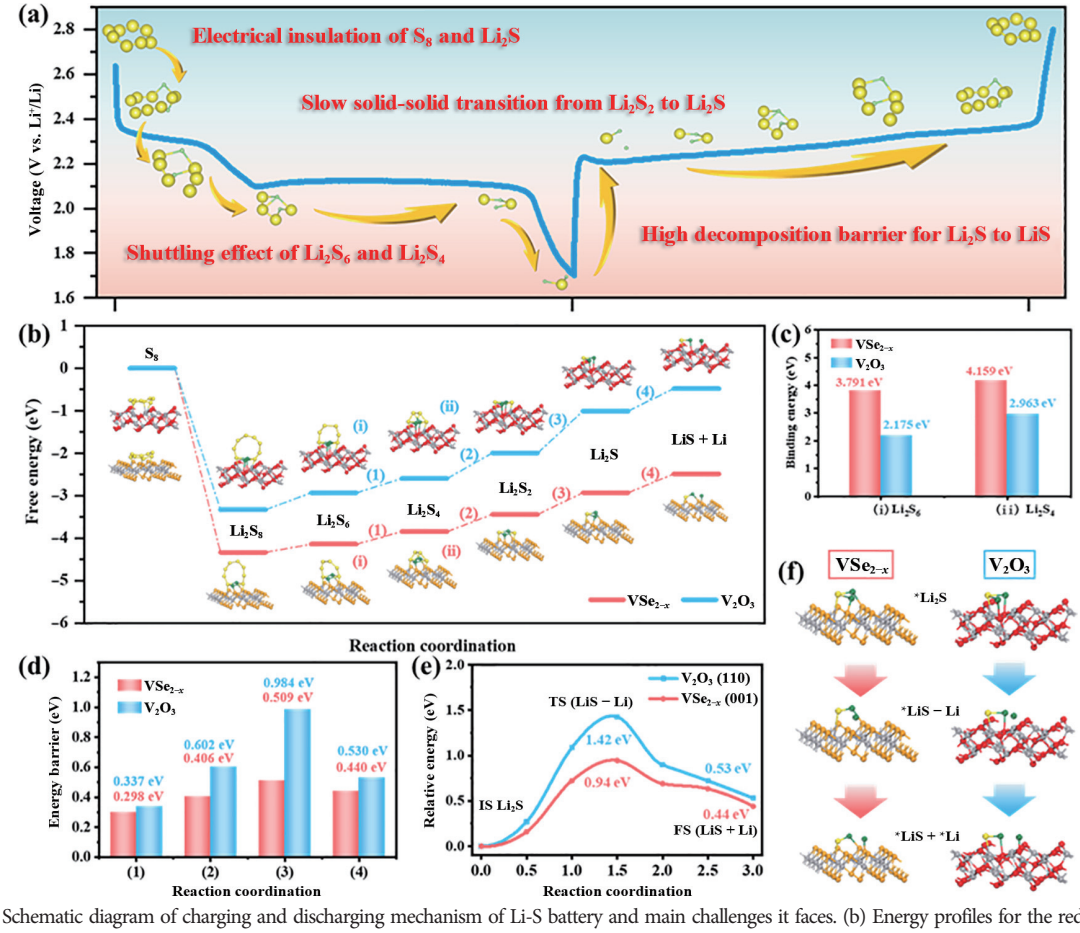

Figure 1 (a) Schematic diagram of charging and discharging mechanism of Li-S battery and main challenges it faces. (b) Energy profiles for the reduction of LiPSs and decomposition of the Li_2S cluster on VSe_{2-x} (001) and V_2O_3 (110). (c) Binding energies of Li_2S_6 and Li_2S_4 on VSe_{2-x} (001) and V_2O_3 (110). (d) The energy profiles required to proceed to steps (1)–(4). The decomposition energy barriers of Li_2S (e) and corresponding optimized configurations (f) on VSe_{2-x} (001) and V_2O_3 (110).

displays stronger anchoring effect on the soluble LiPSs in electrolyte, which effectively inhibits their shuttle effect. On the other hand, VSe_{2-x} shows the greater kinetic enhancements on four key conversion steps than that of V_2O_3, namely the transformation from Li_2S_6 to Li_2S_4-step (1), the transformation from Li_2S_4 to Li_2S_2-step (2), the transformation from Li_2S_2 to Li_2S-step (3), and the transformation from Li_2S to LiS + Li^+-step (4) (Fig. 1(d)). The enhancement of the solid-solid reaction from Li_2S_2 to Li_2S (the rate-limiting step) is undoubtedly the most critical step in a series of sulfur reduction processes [35–37]. Obviously, compared with V_2O_3, VSe_{2-x} shows better sulfur reduction reaction kinetics.

In addition to the sulfur reduction reactions, the sulfur oxidation reactions are also important because they directly determine the charging performance of the battery [38, 39]. The de-lithiation kinetics can be represented by the transformation step from Li_2S to LiS + Li^+. The decomposition energy barriers of Li_2S on VSe_{2-x} (0.44 eV) and V_2O_3 (0.53 eV) are shown in Fig. 1(e) and the corresponding optimized configurations are shown in Fig. 1(f). Obviously, the decomposition energy barrier Li_2S on VSe_{2-x} is much smaller than that on V_2O_3, implying that the greater enhancement on the transformation step from Li_2S to LiS + Li^+ on VSe_{2-x}. Besides, the decomposition energy barrier of Li_2S on VSe_2 (001) without selenium vacancies (about 0.58 eV) is also inferior to VSe_{2-x} [25].

To sum up, it is clear that VSe_{2-x} not only displays stronger anchoring effect on LiPSs, but also shows the greater enhancement on the sulfur redox conversion reactions. It is anticipated that the incorporation of VSe_{2-x} into the N-doped carbon matrix can guarantee high electrode performance for Li-S batteries due to its excellent bidirectional catalytic activity in the redox reactions between Li_2S_n and Li_2S.

3.2 Materials design and preparation

In order to verify our design idea, the NC@VO-VSe was first carefully designed and synthesized via a combined hydrothermal and *in situ* selenization process. As illustrated in Fig. S1 in the Electronic Supplementary Material (ESM), the PVO precursor was prepared through the intercalation and polymerization reaction of aniline in V_2O_5 [40]. Then, through chemical vapor deposition with selenium powder, the NC@VO-VSe was synthesized (Fig. 2). The materials with different proportions of selenide oxides (NC@MVO-VSe and NC@VO-MVSe) can be obtained by controlling the heating process. To prepare the vanadium selenides-rich NC@VO-MVSe composites, a low temperature (350 °C) selenization process is necessary, while a short high temperature annealing process at 500 °C can successfully carbonize the polyaniline into electronic conductive N-doped carbon skeleton. In contrast, directly annealing the PVO precursor at 500 °C for 4 h exacerbates the unwarranted evaporation of the selenium powder, during which the vanadium oxides-rich phase (NC@MVO-VSe) is obtained. The NC@VO was also synthesized by the same calcination process without selenium powder.

To characterize the morphology and phase structure of the materials, a series of morphological characterizations were performed. The unique nanosheets assembled flower like morphology is shown both in typical SEM image of PVO (Fig. 3(a)) and NC@VO-VSe (Fig. 3(b)), indicating the *in situ* selenization process cannot destroy the morphology of PVO precursor. Meanwhile, similar structures can also be seen in typical SEM images of NC@VO (Fig. S2(a) in the ESM), NC@MVO-VSe (Fig. S2(b) in the ESM), and NC@VO-MVSe (Fig. S2(c) in the ESM), further demonstrating the structural stability of the PVO precursor. With a stable flower-like structure (Fig. 3(c)), the NC@VO-VSe sample displays a high specific surface area (46.60 $m^2 \cdot g^{-1}$), a considerable total pore volume (0.332 $cm^3 \cdot g^{-1}$), and abundant mesopores (4–6 nm) (Fig. S3 in the ESM). Meanwhile, the HRTEM images of NC@VO-VSe is revealed in Fig. 3(d), in which two different lattice fringes (0.247 and 0.262 nm) correspond to the (110) crystal face of V_2O_3 and the (001) crystal face of $V_{1.156}Se_2$, respectively. The uniform distribution and the relative content of elements C, N, V, O, and Se can be intuitively reflected in the EDS mapping images (Fig. 3(e)) and TG curve (Fig. 3(f)) of the NC@VO-VSe composite. In TG curve, it can be found that the first weight loss is from room temperature to about 220 °C and the second weight loss is from 220 to 400 °C, indicating the vaporization of 11.66% adsorption water and the

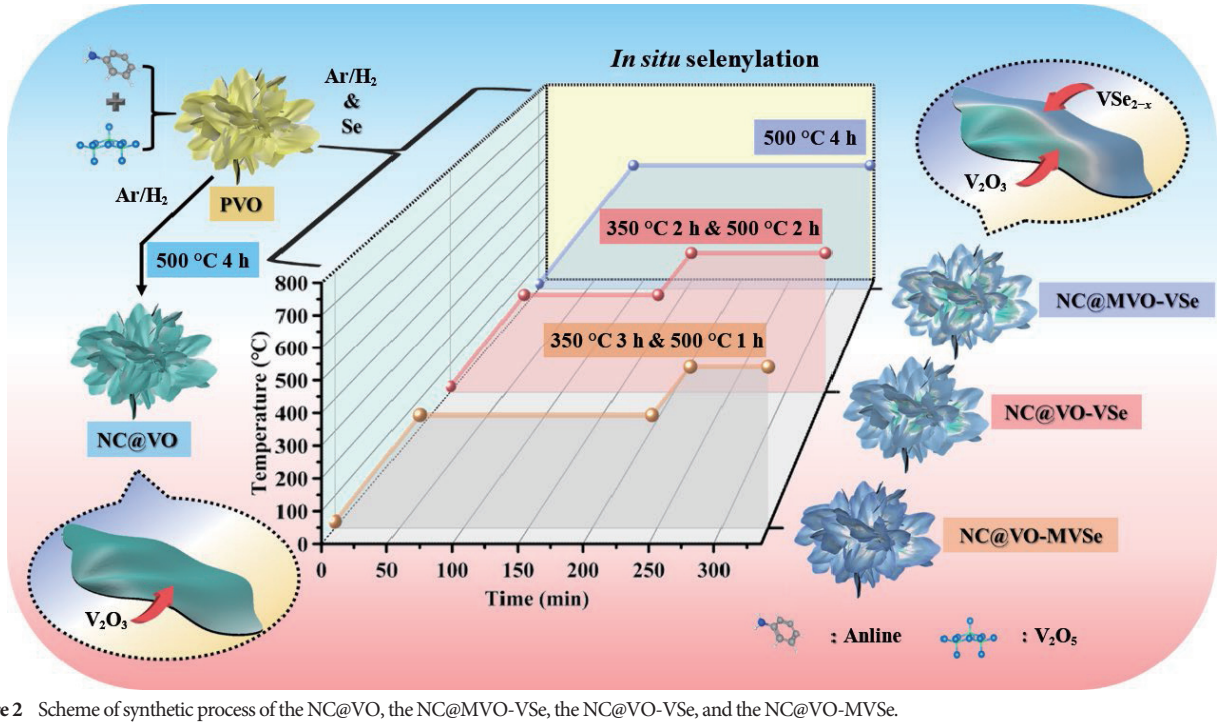

Figure 2 Scheme of synthetic process of the NC@VO, the NC@MVO-VSe, the NC@VO-VSe, and the NC@VO-MVSe.

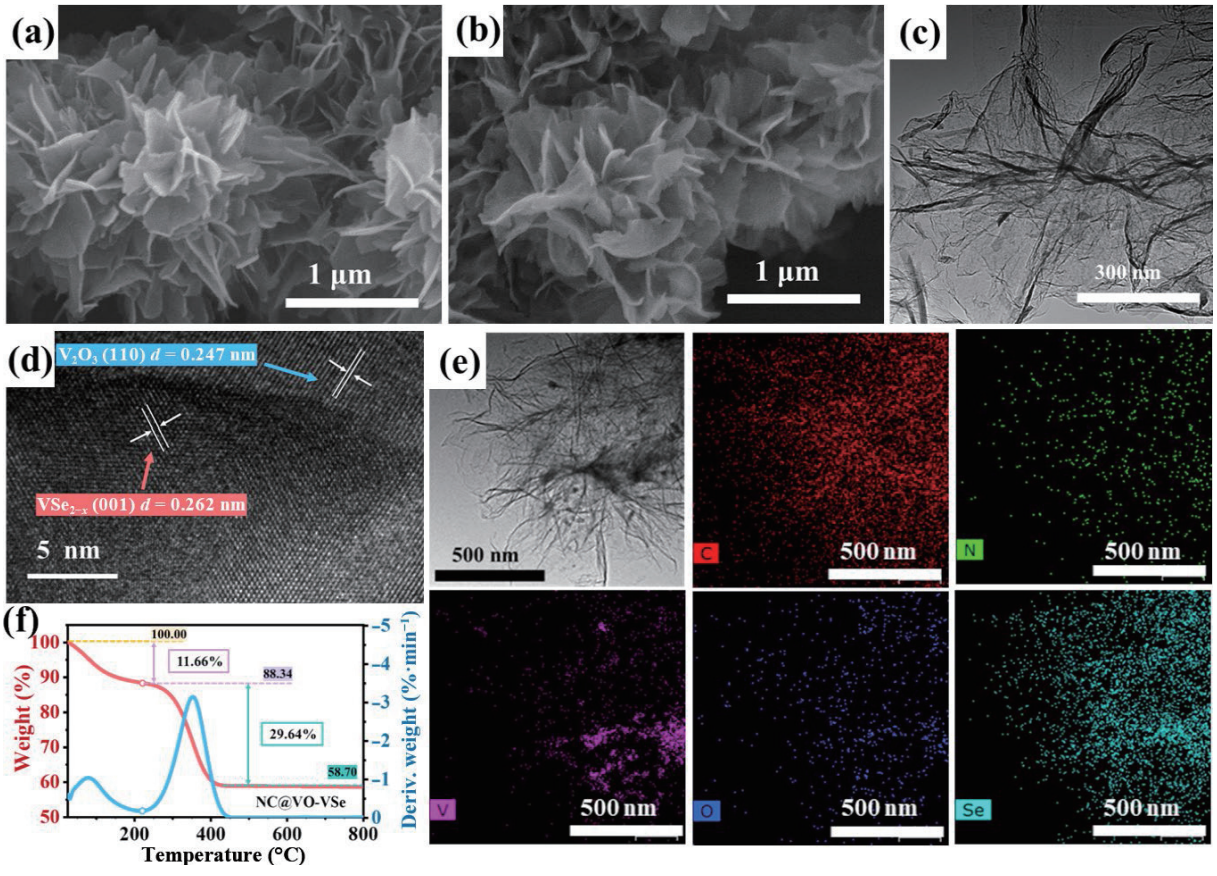

Figure 3 Typical SEM images of (a) PVO and (b) NC@VO-VSe. Typical (c) TEM and (d) HRTEM images of NC@VO-VSe and (e) the corresponding EDS mapping images of C, N, V, O, and Se. (f) TG curve of the NC@VO-VSe composite.

vigorous combustion reactions of the 29.64% carbon component. We can determine the content of VO-VSe in the NC@VO-VSe composite is about 58.70%.

In order to explore the effect of *in situ* selenization under different heating procedures on the composition of the materials, NC@VO, NC@MVO-VSe, NC@VO-VSe, and NC@VO-MVSe were characterized by XRD. The changes in composition of materials can be visualized in Fig. 4(a). The XRD pattern of NC@VO exhibits characteristic peaks corresponding to JCPDS NO. 71-0342 for V_2O_3, whereas the characteristic peaks of both V_2O_3 (PDF 71-0342) and $V_{1.156}Se_2$ (PDF 75-1121) can be found in the XRD patterns of NC@MVO-VSe and NC@VO-VSe, indicating that the *in situ* selenization process can successfully selenize the PVO precursor. The composition proportion is also controllable as indicated by the formation of vanadium selenides-rich phase of NC@VO-MVSe compared to NC@MVO-VSe. It is noteworthy that as one of the important components of the material, $V_{1.156}Se_2$ can be regarded as a non-stoichiometric VSe_{2-x} phase containing selenium vacancies. Interestingly, the low-temperature selenization process forms the NC@VO-MVSe composite, in which the proportion of vanadium selenide exceeds 80% and the characteristic XRD peaks are attributed to the stoichiometric VSe_2 phase rather than $V_{1.156}Se_2$.

More information about the structures of NC@VO and NC@VO-VSe can be obtained by Raman spectra (Fig. 4(b)), in which all peaks of NC@VO can be closely related to V_2O_3. Concretely speaking, the external $[VO_3]$-$[VO_3]$ modes are corresponding to the lower wave number peaks at 98.10 and 156.80 cm^{-1}, while higher wave number peaks at 527.89 and 704.30 cm^{-1} are ascribed to the antiphase bridging V–O and the chaining V–O stretching modes, respectively [41]. As for the NC@VO-VSe sample, the peak at 263.65 cm^{-1} corresponds to the A_{1g} out-of-plane vibration mode of VSe_2 and the peak at 422.44 cm^{-1} corresponds to the E_{2g} in-plane vibration mode. The peaks of NC@VO-VSe shifts to the left due to the decrease of Raman wave number compared with the peaks of NC@VO, which has to do with the bond softening between Se atoms because of the selenium vacancies [42, 43]. In the locally amplified (1,100–1,800) Raman spectra (Fig. 4(c)), two characteristic peaks (about 1,360 and 1,580 cm^{-1}) that correspond to the D and G bands ($I_D/I_G \approx 0.72$) of carbon can be found, indicating both NC@VO-VSe and NC@VO have a low crystallinity of N-doped carbon skeleton.

The surface compositions of the NC@VO-VSe and NC@VO are also investigated using XPS tests. It can be found in Fig. 4(d) that the survey scan XPS spectrum of NC@VO demonstrates the presence of C, N, O, and V elements, while the XPS spectrum of NC@VO-VSe demonstrates the presence of C, N, O, V, and Se elements. The O content in NC@VO-VSe is far less than that in NC@VO. In order to further analyze the composition of selenium, the Se 2d XPS spectra are shown in Fig. 4(e). The peaks at 58.98, 56.08, and 54.68 eV can be indexed to Se–C groups, Se $3d_{3/2}$, and Se $3d_{5/2}$, corresponding to the presence of Se doped carbon and $V_{1.156}Se_2$, respectively [44]. In addition to two peaks (524.58 and 517.38 eV) of V^{4+}, the additional two peaks (523.28 and 516.18 eV) of V^{3+} are also observed in the XPS spectra of V 2p for NC@VO-VSe (Fig. 4(f)), indicating the presence of V^{4+} species in $V_{1.156}Se_2$ and the presence of V^{3+} species in $V_{1.156}Se_2$ and V_2O_3. In Fig. 4(g), the XPS spectrum of C 1s for NC@VO-VSe can be divided into four peaks (288.38, 286.18, 285.18, and 284.68 eV). Specifically, the peak at 288.38 eV can be assigned as C–Se groups, while the peaks at 286.18, 285.18, and 284.68 eV can be indexed to C=O, C–N, and C–C groups, respectively. Moreover, three peaks that can be found in the XPS spectra of O 1s for NC@VO-VSe (Fig. 4(h)) are assigned as C=O, –OH, and V–O groups. In the meantime, the XPS spectra of V 2p, C 1s, and O 1s for NC@VO are exhibited in Fig. S4 in the ESM, and there are only three peaks (287.38, 285.08, and 284.18 eV) in the XPS spectrum of C 1s for NC@VO, being

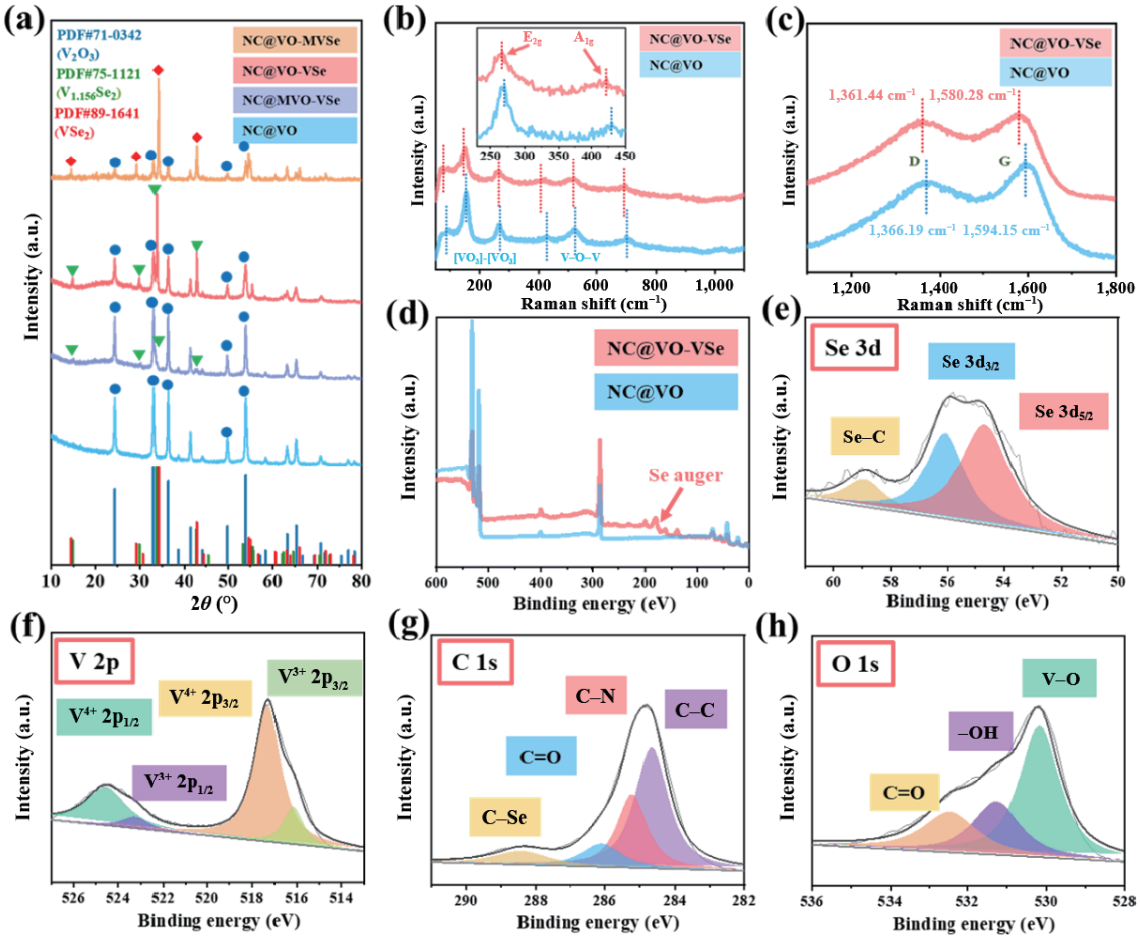

Figure 4 (a) XRD patterns of NC@VO, NC@MVO-VSe, NC@VO-VSe, and NC@VO-MVSe. Locally amplified ((b): 50–1,100; (c): 1,100–1,800) Raman spectra of NC@VO and NC@VO-VSe. (d) Survey scan XPS spectra of NC@VO and NC@VO-VSe. (e) Se 3d, (f) V 2p, (g) C 1s, and (h) O 1s XPS spectra of NC@VO-VSe.

assigned as C=O, C–N, and C–C groups, respectively.

Through the above series of morphology and composition characterizations, NC@VO, NC@MVO-VSe, NC@VO-VSe, and NC@VO-MVSe can be clearly understood. Nanoflowers composed of primary nanosheets are present in all of the above samples. The difference is that NC@MVO-VSe and NC@VO-VSe contain both V_2O_3 and $V_{1.156}Se_2$ with selenium vacancies. However, it is worth noting that the NC@VO-MVSe contains both V_2O_3 and VSe_2. It can be found from the previous theoretical modelling that VSe_{2-x} not only could achieve strong anchoring effect on LiPSs, but also shows the great enhancement on both the sulfur reduction reactions and the sulfur oxidation reactions with the excellent bidirectional catalytic activity in the redox reactions.

3.3 The test of absorption and catalysis to LiPSs

In order to verify the enhancement on both the sulfur reduction reactions and the sulfur oxidation reactions of NC@VO-VSe, symmetrical cells with NC@VO-VSe, NC@VO, and C are assembled. As shown in Fig. 5(a), current response on the CV curve of NC@VO-VSe electrode in Li_2S_6-containing symmetric cells is stronger than that for NC@VO and C. Moreover, in the CV curve of NC@VO-VSe, two couple CV peaks (−0.56/0.56 and −0.25/0.25V) can be found, while only one couple CV peaks (−0.50/0.50 V) are observed in the CV curve of NC@VO. The above results indicate that NC@VO-VSe exhibits stronger LiPSs conversion kinetics than NC@VO. In addition, chronoamperometric curves are used to assess nucleation and growth of Li_2S on NC@VO-VSe, NC@VO, and C. From Fig. 5(b), it can be intuitively found that the peak position of NC@VO-VSe (1,359 s) is earlier than that of NC@VO (2,970 s) and C (4,426 s), as a signal of the more rapid kinetics of Li_2S nucleation. To be specific, as shown in Fig. 5(c), the NC@VO-VSe displays a higher Li_2S electrochemical deposition capacity (167.12 mAh·g^{-1}) than NC@VO (94.98 mAh·g^{-1}) and C (120.51 mAh·g^{-1}). As can be seen from Fig. S5 in the ESM, the deposition of Li_2S on NC@VO-VSe is more uniform than that on NC@VO and C, which can be attributed to the presence of VSe_{2-x}, providing a stronger promotion for the transformation of LiPSs. These results suggest that the incorporation of VSe_{2-x} into the NC@VO-VSe not only accelerates the reaction kinetics of both the sulfur reduction reactions and the sulfur oxidation reactions, but also improves the anchoring effect on LiPSs.

The visual adsorption experiment has been conducted to evaluate the anchoring effect of the catalysts towards LiPSs. Four kinds of Li_2S_6 solutions (pristine LiPS, NC@VO-MVSe/LiPS, NC@VO/LiPS, and C/LiPS) at initial state can be found in Fig. 5(d). It is worth noting that the NC@VO-MVSe composed of VSe_2 is free of selenium vacancies. After 4 h, the NC@VO-based solution becomes colorlessness, while NC@VO-MVSe and C-based solutions show a distinct yellow color. NC@VO-MVSe-based solution approaches to colorless after 10 h, indicating that the anchoring effect of NC@VO-MVSe to LiPSs is inferior to that of NC@VO. Therefore, the adsorption of VSe_2 (without selenium vacancies) to LiPSs is less than that of V_2O_3, while is basically consistent with the theoretical calculation results (VSe_{2-x} to Li_2S_6: 3.791 eV; VSe_{2-x} to Li_2S_4: 4.159 eV; V_2O_3 to Li_2S_6: 2.175 eV; V_2O_3 to Li_2S_4: 2.963 eV; VSe_2 to Li_2S_6: 1.50 eV) [25]. It is anticipated that the synergy of V_2O_3 and VSe_{2-x} strengthens the immobilization of lithium polysulfides, effectively suppressing their shuttle effects.

In summary, VSe_{2-x} exhibits the strongest adsorption effect on

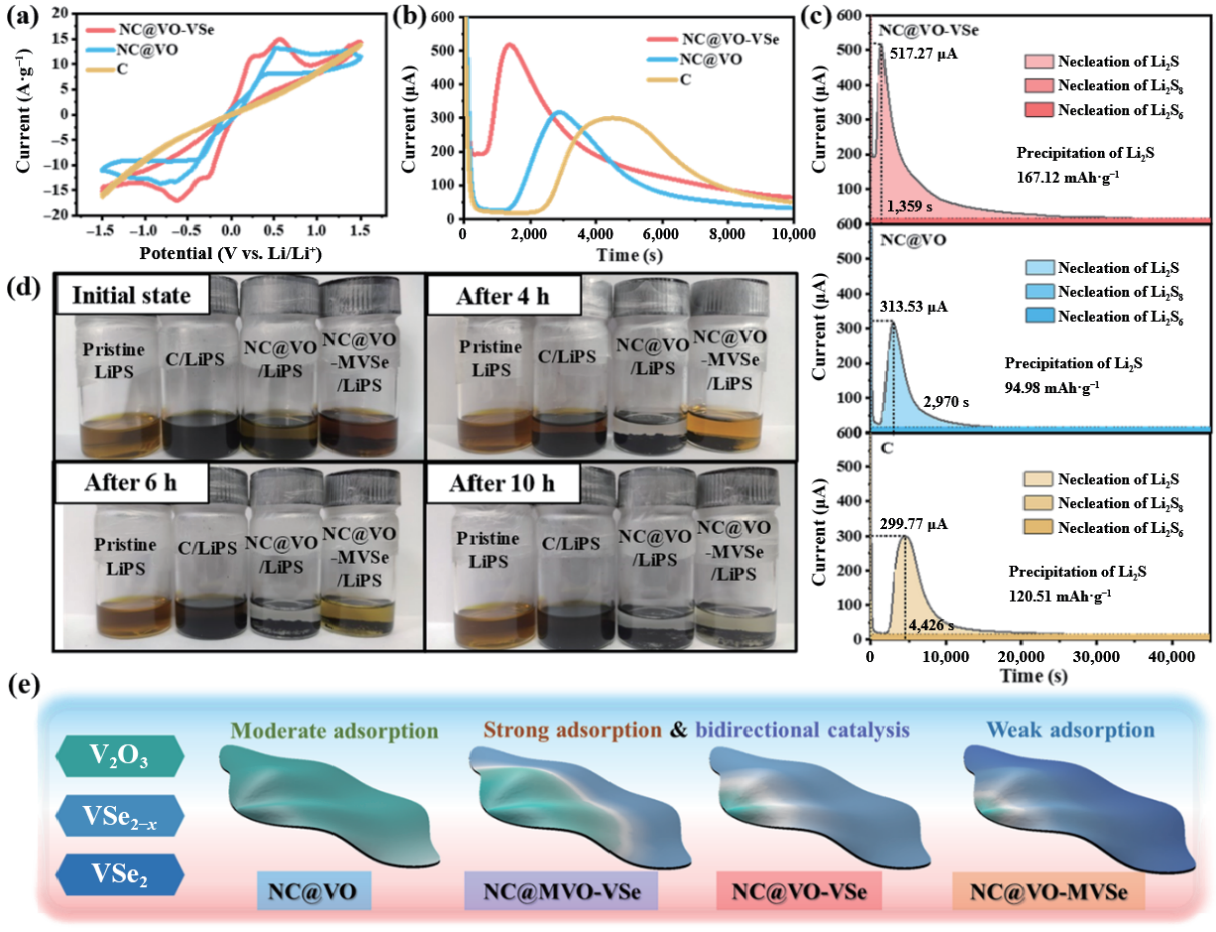

Figure 5 (a) CV curves of symmetrical cells with NC@VO-VSe, NC@VO, and C as working electrodes and the Li_2S_6 solution as electrolyte. (b) and (c) Chronoamperometric curves of Li_2S nucleation tests of NC@VO-VSe, NC@VO, and C. (d) Digital photographs of NC@VO-MVSe, NC@VO, and C soaked in 4 mL 0.5 mM Li_2S_6 solution at the initial state, and after 4, 6, and 10 h. (e) Effects of V_2O_3, VSe_{2-x}, and VSe_2 on LiPSs and compositions of NC@VO, NC@MVO-VSe, NC@VO-VSe, and NC@VO-MVSe.

LiPSs, followed by V_2O_3. VSe_2 displays inferior adsorption effect on LiPSs. As shown in Fig. 5(e), NC@VO shows the moderate adsorption capability towards LiPSs, but its catalytic effect is not obvious. Due to the weak adsorption capacity of VSe_2, NC@VO-MVSe cannot achieve the function of anchoring LiPSs. Compared with the above two samples, NC@VO-VSe not only could achieve strong anchoring effect on LiPSs, but also shows the great kinetic enhancement on both the sulfur reduction and oxidation reactions due to the existence of selenium vacancies.

3.4 Application of the sulfur hosts in Li-S battery

In order to further verify the anchoring effect and great conversion kinetic enhancement towards LiPSs for NC@VO-VSe, the CR2032-type cells are assembled to evaluate the electrochemical performances. The CV curve contains two reduction peaks and an oxidation peak, corresponding to the two-step reduction of S_8 to Li_2S and the one-step transformation of Li_2S to S_8, respectively [45]. The sharpness of oxidation peaks and reduction peaks of CV curve is positively correlated with the discharging and charging kinetics of battery. The sharper oxidation peak represents better charging kinetics, and the sharper reduction peak represents better discharging kinetics. As shown in the CV curves of S/NC@VO-VSe, S/NC@VO, and S/C cathodes (Fig. 6(a)), much sharper and higher peaks (especially reduction peaks) can be seen in the CV curves of S/NC@VO-VSe cathode than the CV curves of S/NC@VO and S/C cathodes, implying that NC@VO-VSe promotes the conversion kinetics (especially discharging kinetics for the reduction process of lithium sulfide). Moreover, the voltage of oxidation peaks and reduction peaks in CV curve is visually shown in Fig. 6(b). Compared to S/NC@VO and S/C cathodes, it can be found that the reduction peaks of S/NC@VO-VSe cathode shift to higher potentials (about 2.0 and 2.3 V) and the oxidation peak shifts to a lower potential (about 2.4 V). This results in a smaller polarization difference in the charge–discharge curve and indicates an enhanced redox kinetics between S_8 and Li_2S. To prove this aspect, the Tafel slopes derived from the cathodic CV peaks (oxidation peaks and reduction peaks) for different cathodes are shown in Fig. S6 in the ESM. It can be found that regardless of the reduction peak or oxidation peak, the Tafel slope derived from CV of NC@VO-VSe is significantly lower than that of NC@VO and C, which further proves the bidirectional catalytic effect of NC@VO-VSe on sulfur species redox reaction. From Fig. S7(a) in the ESM, the first five cycles of CV curves for S/NC@VO-VSe can be intuitively found, and excellent cyclic stability can be clearly implied by a well-overlapped curve. For comparison, the first five cycles of CV curves for S/NC@VO and S/C cathodes are also shown in Figs. S7(b) and S7(c) in the ESM, respectively. Excellent cyclic stability can also be clearly implied by CV curves of S/NC@VO-VSe cathode at different scan rates from 0.1 to 0.5 mV s^{-1} (Fig. 6(c)). There is only a tiny deviation of 0.07 V between CV curves at 0.1 and 0.5 mV·s^{-1}, and the shapes of the CV curves remain basically unchanged as the current density increases. In sharp contrast, more serious deviations (0.13 and 0.09 V) of CV curves for S/NC@VO and S/C cathodes at different scan rates from 0.1 to 0.5 mV·s^{-1} can be found in Figs. S8(a) and S8(b) in the ESM, indicating inferior sulfur conversion kinetics.

As mentioned in the theoretical modelling section, the redox

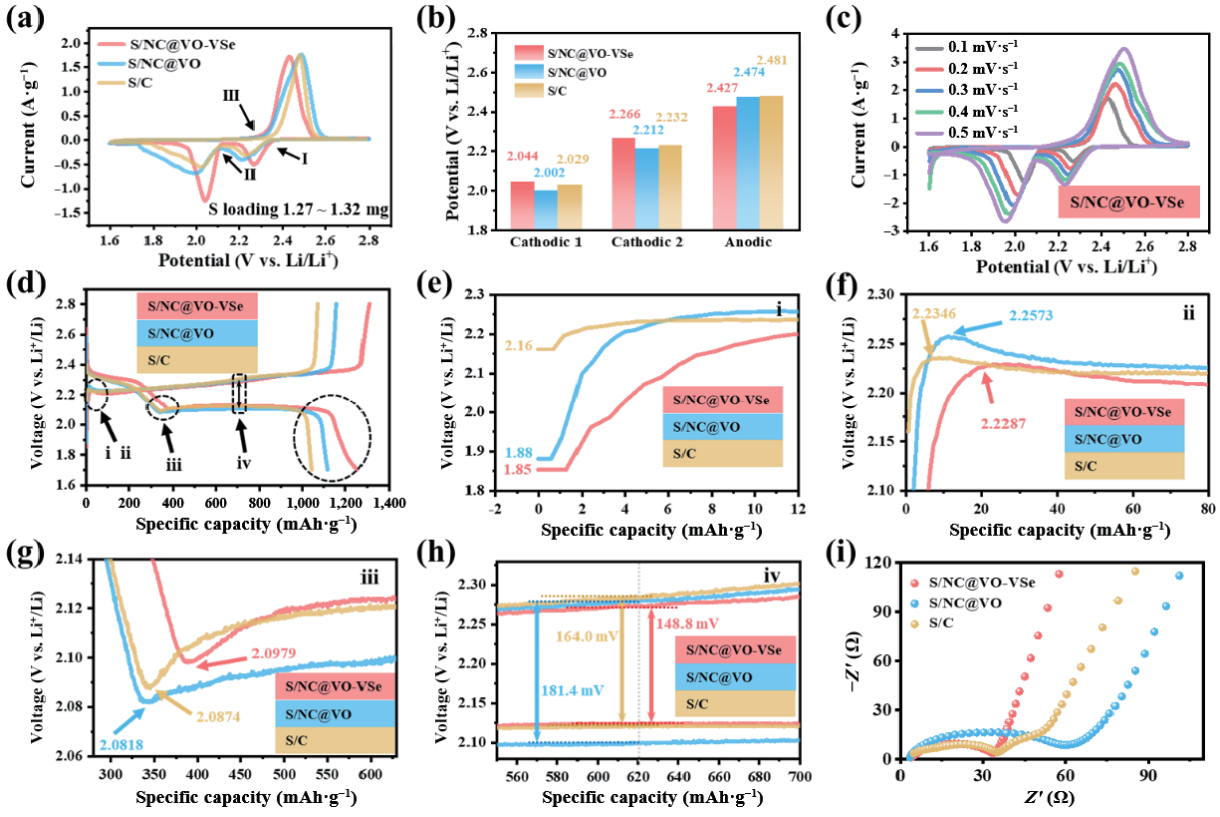

Figure 6 (a) CV curves of cells with S/NC@VO-VSe, S/NC@VO, and S/C cathodes. (b) Voltage of oxidation peaks and reduction peaks in CV curves. (c) CV curves of S/NC@VO-VSe at different scan rates (0.1, 0.2, 0.3, 0.4, and 0.5 mV·s^{-1}). (d) The first charge and discharge profiles of the S/NC@VO-VSe, S/NC@VO, and S/C cathodes at 0.2 C, and (e)–(h) corresponding enlarged part of the galvanostatic charge/discharge curves. (i) EIS spectra of cells of S/NC@VO-VSe, S/NC@VO, and S/C.

kinetics of active substances has a strict one-to-one correspondence with the charge–discharge curve (Fig. 1(a)). Based on this mechanism, several important parameters (Figs. 6(e)–6(h): Initial charging voltage, charging overpotential, discharging overpotential, and voltage difference between charging platform and discharging platform) in the first charge and discharge profiles at 0.2 C (Fig. 6(d)) are shown. In the first charge and discharge profiles of S/NC@VO-VSe cathode at 0.2 C, the lower initial charging voltage (Fig. 6(e), 1.85 V) and the lower overpotential of the charging voltage (Fig. 6(f), 2.23 V) than profiles of S/NC@VO (1.88 and 2.26 V) and S/C (2.16 and 2.23 V) cathodes can be detected, indicating that the energy required for the transformation of Li_2S is significantly reduced for NC@VO-VSe sample.

The overpotential of the discharging voltage can reflect the transformation of Li_2S_6/Li_2S_4 to Li_2S_2. In the first discharge profiles, the lower overpotential of the discharging voltage (Fig. 6(g), 2.10 V) can be detected compared to the S/NC@VO (2.08 V) and S/C (2.09 V) cathodes, indicating that the energy required for the transformation of Li_2S_6/Li_2S_4 is significantly reduced, namely the catalysis of NC@VO-VSe to the so-called "liquid-solid reduction step". From Fig. 6(h), there is a lower polarization potential (ΔE = 148.8 mV) in the charge and discharge profiles of S/NC@VO-VSe cathode than S/NC@VO (ΔE = 181.4 mV) and S/C (ΔE = 164.0 mV) cathodes. In addition, in the discharge profile (Fig. 6(d)), there is a slope after the second platform, corresponding to the transformation from Li_2S_2 to Li_2S [46–49]. The solid-solid reaction kinetics from Li_2S_2 to Li_2S are obviously boosted due to the presence of selenium vacancies in VSe_{2-x}, and the capacity contribution of the ramp part for S/NC@VO-VSe cathode is increased. Moreover, compared to S/NC@VO and S/C cathodes, the S/NC@VO-VSe cathode displays a lower charge transfer resistance and a higher Li-ion migration rate, which can be visually illustrated in Fig. 6(i). The improvement in electronic conductivity and ionic conductivity also promotes the redox kinetics of sulfur to a certain extent [50, 51]. To sum up, it can be adequately revealed by the results that S/NC@VO-VSe cathode shows the great enhancement on both the sulfur reduction reactions and the sulfur oxidation reactions.

To further clarify the catalytic components, the cathodes with different proportions of selenide oxides (S/NC@MVO-VSe and S/NC@VO-MVSe) are also used to evaluate the performance of Li-S battery. It is worth mentioning that S/NC@MVO-VSe cathode has a greater proportion of V_2O_3 than S/NC@VO-VSe cathode, and there is a lot of VSe_2 (vanadium diselselenide without Se vacancies) in S/NC@VO-MVSe cathode. The CV curves of cells with S/NC@MVO-VSe and S/NC@VO-MVSe cathodes are shown in Fig. S9(a) in the ESM. Interestingly, much sharper and higher peaks (especially reduction peaks) can be observed in the CV curves of S/NC@VO-VSe cathode than the CV curves of S/NC@MVO-VSe and S/NC@VO-MVSe cathodes, which implies that compared with S/NC@MVO-VSe and S/NC@VO-MVSe cathodes, the catalytic effect of S/NC@VO-VSe cathode is still obviously superior. The above appeal advantage of S/NC@VO-VSe cathode is also clearly demonstrated by the first charge and discharge profiles of the S/NC@MVO-VSe, S/NC@VO-VSe, and S/NC@VO-MVSe cathodes at 0.2 C. As shown in Figs. S9(b) and S9(c) in the ESM, the S/NC@VO-VSe cathode displays both lower charge and discharge overpotentials than S/NC@MVO-VSe and S/NC@VO-MVSe cathodes. Combined with DFT calculation results, it can be concluded that the above catalytic effect is derived from VSe_{2-x} in the components. On the one hand, due to the existence of selenium vacancies, VSe_{2-x} can promote the liquid-solid transformation from Li_2S_6/Li_2S_4 to Li_2S_2 and the solid-solid transformation from Li_2S_2 to Li_2S, improving the discharge kinetics of Li-S battery. On the other hand, VSe_{2-x} can reduce the decomposition energy barrier of Li_2S, promote the oxidation transformation of Li_2S, and improve the charging kinetics of Li-S

battery.

The rate performances of S/NC@VO-VSe, S/NC@VO, and S/C cathodes are shown in Fig. 7(a). It is clear that the S/NC@VO-VSe cathode displays higher specific discharge capacities (1,256.6, 1,022.8, 922.5, 829.4, 767.2, and 693.7 mAh·g^{-1}) at different current densities (0.2, 0.5, 0.8, 1, 1.5, and 2 C) than the S/NC@VO cathode (0.2 C: 1,160.0 mAh·g^{-1}; 0.5 C: 813.6 mAh·g^{-1}; 0.8 C: 718.8 mAh·g^{-1}; 1 C: 678.8 mAh·g^{-1}; 1.5 C: 626.1 mAh·g^{-1}; 2 C: 579.9 mAh·g^{-1}) and the S/C cathode (0.2 C: 1,072.9 mAh·g^{-1}; 0.5 C: 746.9 mAh·g^{-1}; 0.8 C: 660.6 mAh·g^{-1}; 1 C: 618.1 mAh·g^{-1}; 1.5 C: 566.5 mAh·g^{-1}; 2 C: 539.2 mAh·g^{-1}). Even if the charge and discharge rate recovers to 0.2 C, the S/NC@VO-VSe cathode can still maintain a high specific discharge capacity of 1,115.1 mAh·g^{-1}. By contrast, the capacities of S/NC@VO and S/C are only 814.8 and 725.2 mAh·g^{-1}. The charge and discharge profiles of S/NC@VO-VSe and S/NC@VO cathodes at different rates are shown in Figs. 7(b) and 7(c). The stable charge and discharge profiles can still be maintained for the S/NC@VO-VSe cathode at 2 C. The above results suggest that the cell with S/NC@VO-VSe cathode shows a higher reversible capacity and superior rate property than the S/NC@VO-VSe and S/C cathodes, which is attributed to the adsorption of VSe_{2-x} to LiPSs and the bidirectional catalysis of S_8 to Li_2S. The adsorption of VSe_{2-x} to LiPSs greatly slows down the shuttle effect of LiPSs, while the bidirectional catalysis of S_8 to Li_2S accelerates the transformation between active substances and enhances the kinetics of charge and discharge.

In addition to the above effects, VSe_{2-x} also enhances the cycle performance of Li-S batteries. Figure 7(d) presents the cycle performances of S/NC@VO-VSe, S/NC@VO-VSe, and S/C cathodes. The S/NC@VO-VSe retains a considerable capacity (794.3 mAh·g^{-1}) after 200 cycles at 0.2 C, while the S/NC@VO-VSe and S/C cathodes suffer from short circuit after 114 and 122 cycles, respectively. The charge and discharge profiles of the above three samples after 100 cycles were selected. As shown in Fig. 7(e), the S/NC@VO-VSe retains a considerable capacity (1,025.9 mAh·g^{-1}) and a stable charge and discharge profile after 100 cycles at 0.2 C, while the capacities of S/NC@VO and S/C cathodes decrease dramatically, and the platform shortens seriously. The charge and discharge profiles of the S/NC@VO-VSe, S/NC@VO, and S/C cathodes for different cycles (1st, 5th, 10th, 20th, 50th, and 100th) are shown in Fig. S10 in the ESM. Moreover, cycling performances and Coulombic efficiency (CE) of the S/NC@VO-VSe, S/NC@VO, and S/C cathodes can be seen in Fig. 7(f). A considerable capacity (572.2 mAh·g^{-1}) can be retained for the S/NC@VO-VSe cathode after 400 cycles at 1 C, while the S/C cathode displays an inferior capacity of 177.4 mAh·g^{-1}, and S/NC@VO suffers from short circuit after 277 cycles. In order to prove the structural stabilities of the cathode materials during the cycles, the coin cells are disassembled after 50 cycles (Fig. 8(a)), and the *ex-situ* SEM images of cathodes after 50 cycles are shown in Figs. 8(b)–8(d). Obviously, the electrode surface of S/NC@VO-VSe cathode still remained flat after cycles, while S/NC@VO and S/C cathodes have different degrees of gullies. The above appeal advantage of S/NC@VO-VSe is also clearly demonstrated by the rate performances (Fig. S9(d) in the ESM) and cycling performances (Fig. S9(e) in the ESM) of cells with the S/NC@MVO-VSe, S/NC@VO-VSe, and S/NC@VO-MVSe cathodes, which further indicates the adsorption to LiPSs and the bidirectional catalysis of S_8 to Li_2S by VSe_{2-x}.

Based on current research on Li-S batteries, excellent cycling performance at high rates is of particular importance. As shown in Fig. 8(e), S/NC@VO-VSe cathode has an initial specific capacity of 741 mAh·g^{-1} at 2 C, and it can still maintain 439 mAh·g^{-1} even after 1,000 cycles. The cycling performances of S/NC@VO-VSe cathodes under the different sulfur loading can be found in Fig. S11 in the ESM. Even under 3.07 or even 4.23 mg·cm^{-2} sulfur loading, the batteries can still maintain a relatively stable capacity over 100 cycles. In addition, the influence of the amount of

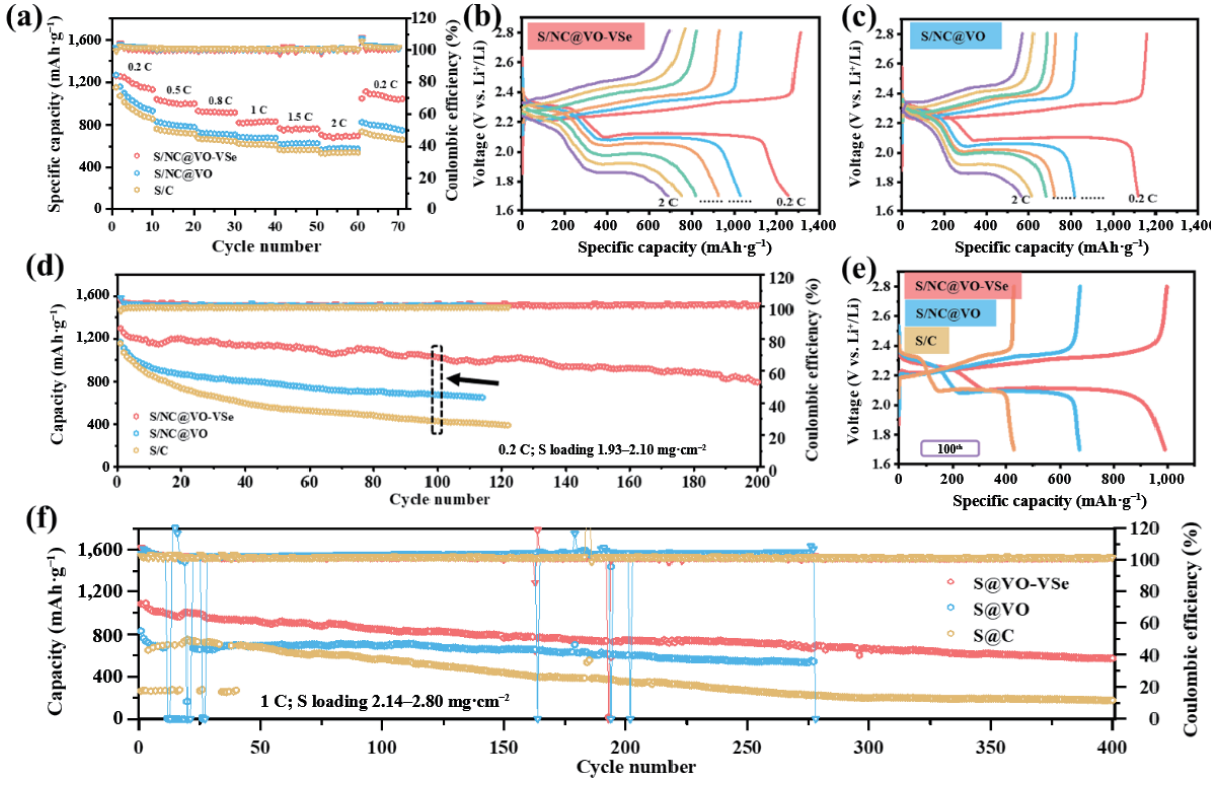

Figure 7 (a) Rate performances of cells with S/NC@VO-VSe, S/NC@VO, and S/C cathodes. The charge and discharge profiles of the S/NC@VO-VSe (b) and S/NC@VO (c) cathodes at different rates (0.2, 0.5, 0.8, 1, 1.5, and 2 C; 1 C = 1675 mA·g^{-1}). (d) Cycling performances and CE of cells with S/NC@VO-VSe, S/NC@VO, and S/C cathodes at 0.2 C. (e) The 100th charge and discharge profiles of S/NC@VO-VSe, S/NC@VO, and S/C cathodes. (f) Cycling performances and CE of cells with S/NC@VO-VSe, S/NC@VO, and S/C cathodes at 1 C.

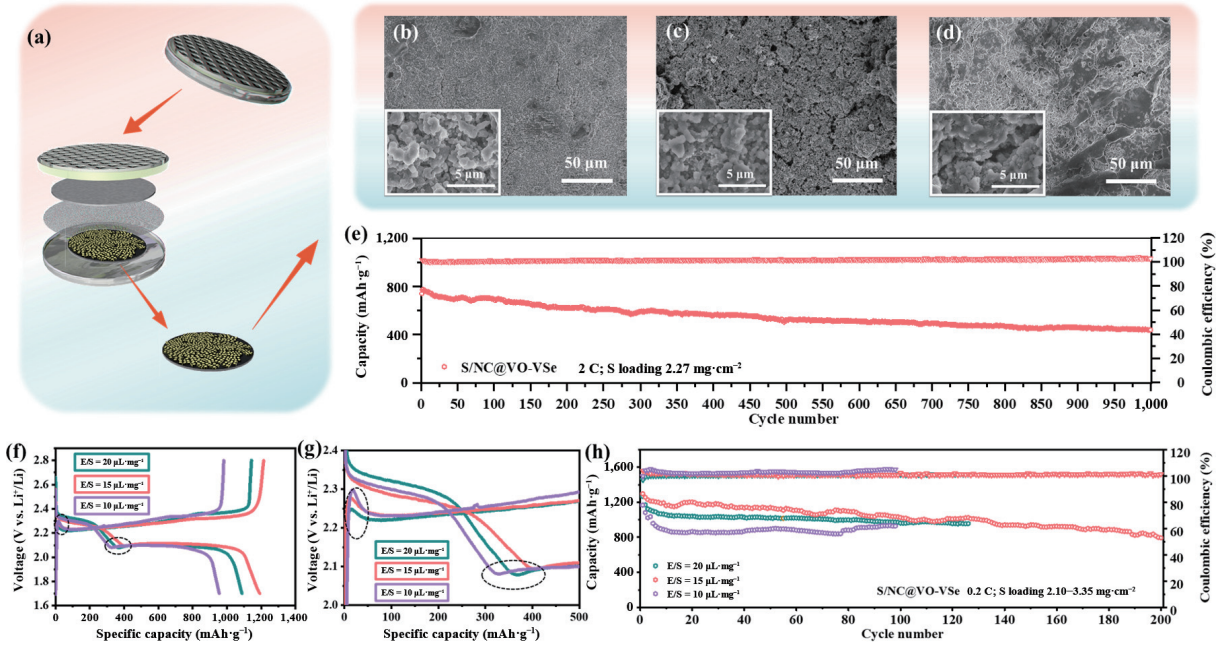

Figure 8 (a) Schematic diagram of cells disassembly after 50 cycles. *Ex-situ* SEM images of S/NC@VO-VSe (b), S/NC@VO (c), and S/C (d) cathodes after 50 cycles. (e) Ultra-long-term cycling performances and CE of cells with S/NC@VO-VSe cathode at 2 C. (f) The 5th charge and discharge profiles of the S/NC@VO-VSe cathode with the different electrolyte/sulfur ratio (20, 15, and 10 μL·mg^{-1}) at 0.2 C, corresponding enlarged part of the galvanostatic charge/discharge curves (g), and corresponding cycling performances and CE (h).

electrolyte on the charge/discharge dynamics and the cycle performance of the cathode is also investigated. The 5th charge and discharge profiles of the S/NC@VO-VSe cathode with the different electrolyte/sulfur (E/S) ratio (20, 15, and 10 μL·mg^{-1}) at 0.2 C are shown in Figs. 8(f) and 8(g). Compared with the S/NC@VO-VSe cathode with 15 μL·mg^{-1} (E/S ratio), although the S/NC@VO-VSe cathode with 20 μL·mg^{-1} exhibits better charging dynamics, it displays lower specific capacity. A small excess electrolyte can promote the charging kinetic to a certain extent. However, it also promotes shuttle effect of LiPSs, resulting in the loss of active substances. The cell with low E/S ratio requires long cycles to reactivate the sulfur species to achieve a substantial specific capacity (Fig. 8(h)). At the same time, the lean electrolyte will lead to slow charge/discharge dynamics of the battery, which can be seen intuitively in Fig. 8(g). Based on the above results, appropriate electrolyte (appropriate E/S ratio) is particularly important for improving battery performance.

Due to selenium vacancies, VSe_{2-x} displays a stronger adsorption on LiPSs. At the same time, the energy barrier in the redox conversion process of active substances is greatly reduced, and the kinetics of charge and discharge of Li-S battery is fundamentally improved. Correspondingly, V_2O_3 has a moderate adsorption on LiPSs, while VSe_2 has a weak adsorption on LiPSs. Adsorption of different intensities results in the difference in the ability of S/NC@VO, S/NC@MVO-VSe, S/NC@VO-VSe, and S/NC@VO-MVSe cathodes to inhibit the LiPSs shuttle effect (Fig. 5(e)). Concretely speaking, S/NC@VO and S/NC@VO-MVSe cathodes lack sufficient adsorption, and the proportion of VSe_{2-x} in S/NC@MVO-VSe cathode is lower than the proportion of VSe_{2-x} in S/NC@VO-VSe cathode. To sum up, the cell with S/NC@VO-VSe cathode has an outstanding redox kinetic and cyclic stability.

4 Conclusions

In summary, the stronger adsorption to LiPSs and the bidirectional catalysis of the conversion between S_8 and Li_2S by the VSe_{2-x} with selenium vacancies have been demonstrated for the first time at the molecular scale through DFT calculations. The NC@VO-VSe composite has been controllably synthesized via a combined hydrothermal and *in situ* selenization process. Benefited from sufficient selenium vacancies in VSe_{2-x}, the NC@VO-VSe presents a stronger adsorption on LiPSs, which effectively inhibits their shuttle effect. Besides, the NC@VO-VSe displays the bidirectional catalysis on the sulfur conversion reactions. The energy barriers in the redox process of active substances are greatly reduced, and the charge and discharge kinetics are fundamentally improved. The cell with S/NC@VO-VSe cathode exhibits an excellent charge and discharge kinetics, an outstanding rate capability of 693.7 mAh·g^{-1} at 2 C, and a remarkable long-term cyclability for 400 cycles at 1 C with S loading 2.8 mg·cm^{-2}. The effective deficiency engineering approaches to couple the adsorbability and catalytic reactions of LiPSs, and the bidirectional catalytic functionality is insightful for the development of electrode materials for next generation Li-S battery technologies.

Acknowledgements

This work was supported by the National Natural Science Foundation of China (No. 51972187), the Natural Science Foundation of Shandong Province (Nos. ZR2021QE166 and ZR2019MB037), the Project funded by China Postdoctoral Science Foundation (No. 2021M701817), and the Major Basic Research Program of Natural Science Foundation of Shandong Province (No. ZR2020ZD09).

Electronic Supplementary Material: Supplementary material (further details of the SEM measurements, TEM imaging, and electrochemistry measurements) is available in the online version of this article at https://doi.org/10.1007/s12274-022-4552-7.

References

[1] Zhou, G. M.; Yang, A. K.; Gao, G. P.; Yu, X. Y.; Xu, J. W.; Liu, C. W.; Ye, Y. S.; Pei, A.; Wu, Y.; Peng, Y. C. et al. Supercooled liquid sulfur maintained in three-dimensional current collector for high-performance Li-S batteries. *Sci. Adv.* **2020**, *6*, eaay5098.

[2] Yang, A. K.; Zhou, G. M.; Kong, X.; Vilá, R. A.; Pei, A.; Wu, Y. C.;

Yu, X. Y.; Zheng, X. L.; Wu, C. L.; Liu, B. F. et al. Electrochemical generation of liquid and solid sulfur on two-dimensional layered materials with distinct areal capacities. *Nat. Nanotechnol.* **2020**, *15*, 231–237.

[3] Ye, J. C.; Chen, J. J.; Yuan, R. M.; Deng, D. R.; Zheng, M. S.; Cronin, L.; Dong, Q. F. Strategies to explore and develop reversible redox reactions of Li-S in electrode architectures using silver-polyoxometalate clusters. *J. Am. Chem. Soc.* **2018**, *140*, 3134–3138.

[4] Tsao, Y.; Lee, M.; Miller, E. C.; Gao, G. P.; Park, J.; Chen, S. C.; Katsumata, T.; Tran, H.; Wang, L. W.; Toney, M. F. et al. Designing a quinone-based redox mediator to facilitate Li_2S oxidation in Li-S batteries. *Joule* **2019**, *3*, 872–884.

[5] Wang, L.; Liu, S. K.; Hu, J.; Zhang, X. N.; Li, X.; Zhang, G. H.; Li, Y. J.; Zheng, C. M.; Hong, X. B.; Duan H. G. Tailoring polysulfide trapping and kinetics by engineering hollow carbon bubble nanoreactors for high-energy Li-S pouch cells. *Nano Res.* **2021**, *14*, 1355–1363.

[6] Hu, A. J.; Zhou, M. J.; Lei, T. Y.; Hu, Y.; Du, X. C.; Gong, C. H.; Shu, C. Z.; Long, J. P.; Zhu, J.; Chen, W. et al. Optimizing redox reactions in aprotic lithium-sulfur batteries. *Adv. Energy Mater.* **2020**, *10*, 2002180.

[7] Yan, X. J.; Guo, W. Q.; Li, W. D.; Li, G. L.; Yue, Z. J.; Liu, J.; Peng, H. R.; Yin, Z. M.; Zhang, Z. H.; Mao, C. M. et al. Coupling highly dispersed Sb_2S_3 nanodots with nitrogen/sulfur dual-doped porous carbon nanosheets for efficient immobilization and catalysis of polysulfides conversion. *Chem. Eng. J.* **2021**, *420*, 127688.

[8] Pang, Q.; Shyamsunder, A.; Narayanan, B.; Kwok, C. Y.; Curtiss, L. A.; Nazar, L. F. Tuning the electrolyte network structure to invoke quasi-solid state sulfur conversion and suppress lithium dendrite formation in Li-S batteries. *Nat. Energy* **2018**, *3*, 783–791.

[9] Lei, T. Y.; Chen, W.; Lv, W. Q.; Huang, J. W.; Zhu, J.; Chu, J. W.; Yan, C. Y.; Wu, C. Y.; Yan, Y. C.; He, W. D. et al. Inhibiting polysulfide shuttling with a graphene composite separator for highly robust lithium-sulfur batteries. *Joule* **2018**, *2*, 2091–2104.

[10] Liu, B. R.; Taheri, M.; Torres, J. F.; Fusco, Z.; Lu, T.; Liu, Y.; Tsuzuki, T.; Yu, G. H.; Tricoli, A. Janus conductive/insulating microporous ion-sieving membranes for stable Li-S batteries. *ACS Nano* **2020**, *14*, 13852–13864.

[11] Zhang, F.; Guo, X.; Xiong, P.; Zhang, J. Q.; Song, J. J.; Yan, K.; Gao, X. C.; Liu, H.; Wang, G. X. Interface engineering of MXene composite separator for high-performance Li-Se and Na-Se batteries. *Adv. Energy Mater.* **2020**, *10*, 2000446.

[12] Cha, E.; Patel, M. D.; Park, J.; Hwang, J.; Prasad, V.; Cho, K.; Choi, W. 2D MoS_2 as an efficient protective layer for lithium metal anodes in high-performance Li-S batteries. *Nat. Nanotechnol.* **2018**, *13*, 337–344.

[13] Pang, Q.; Kwok, C. Y.; Kundu, D.; Liang, X.; Nazar, L. F. Lightweight metallic MgB_2 mediates polysulfide redox and promises high-energy-density lithium-sulfur batteries. *Joule* **2019**, *3*, 136–148.

[14] Zhou, J. B.; Liu, X. J.; Zhu, L. Q.; Zhou, J.; Guan, Y.; Chen, L.; Niu, S. W.; Cai, J. Y.; Sun, D.; Zhu, Y. C. Deciphering the modulation essence of p bands in Co-based compounds on Li-S chemistry. *Joule* **2018**, *2*, 2681–2693.

[15] Li, Y. C.; Li, W. D.; Yan, X. J.; Zhou, Z. F.; Guo, X. S.; Liu, J.; Mao, C. M.; Zhang, Z. H.; Li, G. C. Terminal sulfur atoms formation via defect engineering strategy to promote the conversion of lithium polysulfides. *J. Mater. Sci. Technol.* **2022**, *103*, 221–231.

[16] Chen, H.; Zhou, G. M.; Boyle, D.; Wan, J. Y.; Wang, H. X.; Lin, D. C.; Mackanic, D.; Zhang, Z. W.; Kim, S. C.; Lee, H. R. et al. Electrode design with integration of high tortuosity and sulfur-philicity for high-performance lithium-sulfur battery. *Matter* **2020**, *2*, 1605–1620.

[17] Wang, Z. K.; Ji, H. Q.; Zhou, L. Z.; Shen, X. W.; Gao, L. H.; Liu, J.; Yang, T. Z.; Qian, T.; Yan, C. L. All-liquid-phase reaction mechanism enabling cryogenic Li-S batteries. *ACS Nano* **2021**, *15*, 13847–13856.

[18] Li, W. D.; Wang, D. Z.; Song, Z. H.; Gong Z. J.; Guo, X. S.; Liu, J.; Zhang, Z. H.; Li, G. C. Carbon confinement synthesis of interlayer-expanded and sulfur-enriched MoS_{2+x} nanocoating on hollow carbon spheres for advanced Li-S batteries. *Nano Res.* **2019**, *12*, 2908–2917.

[19] Wang, T.; Zhu, J.; Wei, Z. X.; Yang, H. G.; Ma, Z. L.; Ma, R. F.; Zhou, J.; Yang, Y. H.; Peng, L. L.; Fei, H. L. et al. Bacteria-derived biological carbon building robust Li-S batteries. *Nano Lett.* **2019**, *19*, 4384–4390.

[20] Ye, C.; Jiao, Y.; Jin, H. Y.; Slattery, A. D.; Davey, K.; Wang, H. H.; Qiao, S. Z. 2D MoN-VN heterostructure to regulate polysulfides for highly efficient lithium-sulfur batteries. *Angew. Chem., Int. Ed.* **2018**, *57*, 16703–16707.

[21] Zhang, B.; Luo, C.; Deng, Y. Q.; Huang, Z. J.; Zhou, G. M.; Lv, W.; He, Y. B.; Wan, Y.; Kang, F. Y.; Yang, Q. H. Optimized catalytic WS_2-WO_3 heterostructure design for accelerated polysulfide conversion in lithium-sulfur batteries. *Adv. Energy Mater.* **2020**, *10*, 2000091.

[22] Song, Y. Z.; Zhao, W.; Kong, L.; Zhang, L.; Zhu, X. Y.; Shao, Y. L.; Ding, F.; Zhang, Q.; Sun, J. Y.; Liu, Z. F. Synchronous immobilization and conversion of polysulfides on a VO_2-VN binary host targeting high sulfur load Li-S batteries. *Energy Environ. Sci.* **2018**, *11*, 2620–2630.

[23] Zhang, L.; Liu, Y. C.; Zhao, Z. D.; Jiang, P. L.; Zhang, T.; Li, M. X.; Pan, S. X.; Tang, T. Y.; Wu, T. Q.; Liu, P. Y. et al. Enhanced polysulfide regulation via porous catalytic V_2O_3/V_8C_7 heterostructures derived from metal–organic frameworks toward high-performance Li-S batteries. *ACS Nano* **2020**, *14*, 8495–8507.

[24] He, J. R.; Bhargav, A.; Manthiram, A. Molybdenum boride as an efficient catalyst for polysulfide redox to enable high-energy-density lithium-sulfur batteries. *Adv. Mater.* **2020**, *32*, 2004741.

[25] Tian, W. Z.; Xi, B. J.; Gu, Y.; Fu, Q.; Feng, Z. Y.; Feng, J. K.; Xiong, S. L. Bonding VSe_2 ultrafine nanocrystals on graphene toward advanced lithium-sulfur batteries. *Nano Res.* **2020**, *13*, 2673–2682.

[26] Shen, Z. H.; Zhang, Z. L.; Li, M.; Yuan, Y. F.; Zhao, Y.; Zhang, S.; Zhong, C. L.; Zhu, J.; Lu, J.; Zhang, H. G. Rational design of a $Ni_3N_{0.85}$ electrocatalyst to accelerate polysulfide conversion in lithium-sulfur batteries. *ACS Nano* **2020**, *14*, 6673–6682.

[27] Zou, Y. H.; Gu, Y.; Hui, B.; Yang, X. F.; Liu, H. W.; Chen, S.; Cai, R. S.; Sun, J.; Zhang, X. L.; Yang, D. J. Nitrogen and sulfur vacancies in carbon shell to tune charge distribution of $Co_6Ni_3S_8$ core and boost sodium storage. *Adv. Energy Mater.* **2020**, *10*, 1904147.

[28] Yang, Q. F.; Cui, M. N.; Hu, J. L.; Chu, F. L.; Zheng, Y. J.; Liu, J. J.; Li, C. L. Ultrathin defective C–N coating to enable nanostructured Li plating for Li metal batteries. *ACS Nano* **2020**, *14*, 1866–1878.

[29] Li, Y.; Qian, J.; Zhang, M. H.; Wan, S.; Wang, Z. H.; Li, M. S.; Bai, Y.; An, Q. Y.; Xu, H. J.; Wu, F. et al. Co-construction of sulfur vacancies and heterojunctions in tungsten disulfide to induce fast electronic/ionic diffusion kinetics for sodium-ion batteries. *Adv. Mater.* **2020**, *32*, 2005802.

[30] Kresse, G.; Furthmüller, J. Efficiency of *ab-initio* total energy calculations for metals and semiconductors using a plane-wave basis set. *Comput. Mater. Sci.* **1996**, *6*, 15–50.

[31] Kresse, G.; Furthmüller, J. Efficient iterative schemes for *ab initio* total-energy calculations using a plane-wave basis set. *Phys. Rev. B* **1996**, *54*, 11169–11186.

[32] Perdew, J. P.; Burke, K.; Ernzerhof, M. Generalized gradient approximation made simple. *Phys. Rev. Lett.* **1996**, *77*, 3865–3868.

[33] Kresse, G.; Joubert, D. From ultrasoft pseudopotentials to the projector augmented-wave method. *Phys. Rev. B* **1999**, *59*, 1758–1775.

[34] Blöchl, P. E. Projector augmented-wave method. *Phys. Rev. B* **1994**, *50*, 17953–17979.

[35] Li, Y. J.; Wang, W. Y.; Zhang, B.; Fu, L.; Wan, M. T.; Li, G. C.; Cai, Z.; Tu, S. B.; Duan, X. R.; Seh, Z. W. et al. Manipulating redox kinetics of sulfur species using Mott-Schottky electrocatalysts for advanced lithium-sulfur batteries. *Nano Lett.* **2021**, *21*, 6656–6663.

[36] Hu, A. J.; Chen, W.; Du, X. C.; Hu, Y.; Lei, T. Y.; Wang, H. B.; Xue, L. X.; Li, Y. Y.; Sun, H.; Yan, Y. C. et al. An artificial hybrid interphase for an ultrahigh-rate and practical lithium metal anode. *Energy Environ. Sci.* **2021**, *14*, 4115–4124.

[37] Ni, L. B.; Yang, G.; Liu, Y.; Wu, Z.; Ma, Z. Y.; Shen, C.; Lv, Z. X.; Wang, Q.; Gong, X. X.; Xie, J. et al. Self-assembled polyoxometalate nanodots as bidirectional cluster catalysts for

polysulfide/sulfide redox conversion in lithium-sulfur batteries. *ACS Nano* **2021**, *15*, 12222–12236.

[38] Yu, B.; Huang, A. J.; Srinivas, K.; Zhang, X. J.; Ma, F.; Wang, X. Q.; Chen, D. J.; Wang, B.; Zhang, W. L.; Wang, Z. G. et al. Outstanding catalytic effects of 1T'-$MoTe_2$ quantum dots@3D graphene in shuttle-free Li-S batteries. *ACS Nano* **2021**, *15*, 13279–13288.

[39] Ye, Z. Q.; Jiang, Y.; Yang, T. Y.; Li, L.; Wu, F.; Chen, R. J. Engineering catalytic CoSe-ZnSe heterojunctions anchored on graphene aerogels for bidirectional sulfur conversion reactions. *Adv. Sci.* **2022**, *9*, 2103456.

[40] Zeng, J.; Zhang, Z. H.; Guo, X. S.; Li, G. C. A conjugated polyaniline and water co-intercalation strategy boosting zinc-ion storage performances for rose-like vanadium oxide architectures. *J. Mater. Chem. A* **2019**, *7*, 21079–21084.

[41] Zakharova, G. S.; Thauer, E.; Enyashin, A. N.; Deeg, L. F.; Zhu, Q.; Klingeler, R. V_2O_3/C composite fabricated by carboxylic acid-assisted sol-gel synthesis as anode material for lithium-ion batteries. *J. Sol-Gel Sci. Technol.* **2021**, *98*, 549–558.

[42] Li, D.; Wang, X.; Kan, C. M.; He, D. L.; Li, Z. J.; Hao, Q.; Zhao, H. B.; Wu, C. Z.; Jin, C. H.; Cui, X. D. Structural phase transition of multilayer VSe_2. *ACS Appl. Mater. Interfaces* **2020**, *12*, 25143–25149.

[43] Chen, Y. P.; Yang, G.; Zhang, Z. H.; Yang, X. Y.; Hou, W. H.; Zhu, J. J. Polyaniline-intercalated layered vanadium oxide nanocomposites-one-pot hydrothermal synthesis and application in lithium battery. *Nanoscale* **2010**, *2*, 2131–2138.

[44] Kim, J. K.; Kang, Y. C. Encapsulation of Se into hierarchically porous carbon microspheres with optimized pore structure for advanced Na-Se and K-Se batteries. *ACS Nano* **2020**, *14*, 13203–13216.

[45] Ma, C.; Zhang, Y. Q.; Feng, Y. M.; Wang N.; Zhou, L. J.; Liang, C. P.; Chen, L. B.; Lai, Y. Q.; Ji, X. B.; Yan, C. L. et al. Engineering Fe–N coordination structures for fast redox conversion in lithium-sulfur batteries. *Adv. Mater* **2021**, *33*, 2100171.

[46] Jin, Z. S.; Lin, T. N.; Jia, H. F.; Liu, B. Q.; Zhang, Q.; Li, L.; Zhang, L. Y.; Su, Z. M.; Wang, C. G. Expediting the conversion of Li_2S_2 to Li_2S enables high-performance Li-S batteries. *ACS Nano* **2021**, *15*, 7318–7327.

[47] Huang, S. Z.; Wang, Y.; Hu, J. P.; Lim, Y. V.; Kong, D. Z.; Guo, L.; Kou, Z. K.; Chen, Y. X.; Yang, H. Y. *In situ*-grown compressed $NiCo_2S_4$ barrier layer for efficient and durable polysulfide entrapment. *NPG Asia Mater.* **2019**, *11*, 55.

[48] Wu, L. C.; Gu, M. Y.; Feng, Y. H.; Chen, S. H.; Fan, L.; Yu, X. Z.; Guo, K. K.; Zhou, J.; Lu, B. G. Layered superconductor $Cu_{0.11}TiSe_2$ as a high-stable K-cathode. *Adv. Funct. Mater.* **2022**, *32*, 2109893.

[49] Ge, J. M.; Fan, L.; Rao, A. M.; Zhou, J.; Lu, B. G. Surface-substituted Prussian blue analogue cathode for sustainable potassium-ion batteries. *Nat. Sustain.* **2022**, *5*, 225–234.

[50] Li, Y. C.; Yan, X. J.; Zhou, Z. F.; Liu, J.; Zhang, Z. H.; Guo, X. S.; Peng, H. R.; Li, G. C. Synergistic coupling between Fe_7S_8-MoS_2 heterostructure and few layers MoS_2-embeded N-/P-doping carbon nanocapsule enables superior Li-S battery performances. *Appl. Surf. Sci.* **2022**, *574*, 151586.

[51] Ci, H. N.; Cai, J. S.; Ma, H.; Shi, Z. X.; Cui, G.; Wang, M. L.; Jin, J.; Wei, N.; Lu, C.; Zhao, W. et al. Defective VSe_2-graphene heterostructures enabling *in situ* electrocatalyst evolution for lithium-sulfur batteries. *ACS Nano* **2020**, *14*, 11929–11938.